5 SCIENTIFIC HIGHLIGHT OF THE MONTH: Advancing DFT to finite temperatures: Methods and applications in steel design

Advancing DFT to finite temperatures: Methods and applications in steel design
T. Hickel, B. Grabowski*, F. Körmann and J. Neugebauer
Max-Planck-Institut für Eisenforschung GmbH (MPIE), Düsseldorf, Germany
**now at: Lawrence Livermore National Laboratory (LLNL)*

Abstract

The performance of materials such as steels, their high strength and formability, is based on an impressive variety of competing mechanisms on the microscopic/atomic scale (e.g., dislocation gliding, solid solution hardening, mechanical twinning or structural phase transformations). Whereas many of the currently available concepts to describe these mechanisms are based on empirical and experimental data, it becomes more and more apparent that further improvement of materials needs to be based on a more fundamental level. Recent progress in the field of *ab initio* methods makes now the exploration of chemical trends, the determination of parameters for phenomenological models, and the identification of new routes for the optimization of steel properties feasible. A major challenge in applying these methods to a true materials design is, however, the inclusion of temperature driven effects on the desired properties. Therefore, a large range of computational tools has been developed in order to improve the capability and accuracy of first-principles methods in determining free energies. These combine electronic, vibrational, and magnetic effects as well as structural defects in an integrated approach. Based on these simulation tools, one is now able to successfully predict mechanical and thermodynamic properties of metals with a hitherto not achievable accuracy.

1 Introduction

1.1 Motivation

The fascinating world of materials design covers a large variety of physical quantities that need to be optimized for special applications. In steel design the focus is very often on mechanical properties, their strength and ductility. For the latter two quantities an inverse relation is often observed visualized in Fig. 1: On the one hand, some ferritic steels allow huge elongations of more than 50% before fracture, suffering however from a low ultimate tensile strength. On the other hand, much higher strength levels can be obtained by, e.g., martensitic steels, but this time at the expense of low accessible deformation rates. For many applications, in particular in automotive industry, a combination of high ductility and high strength is highly desirable. For

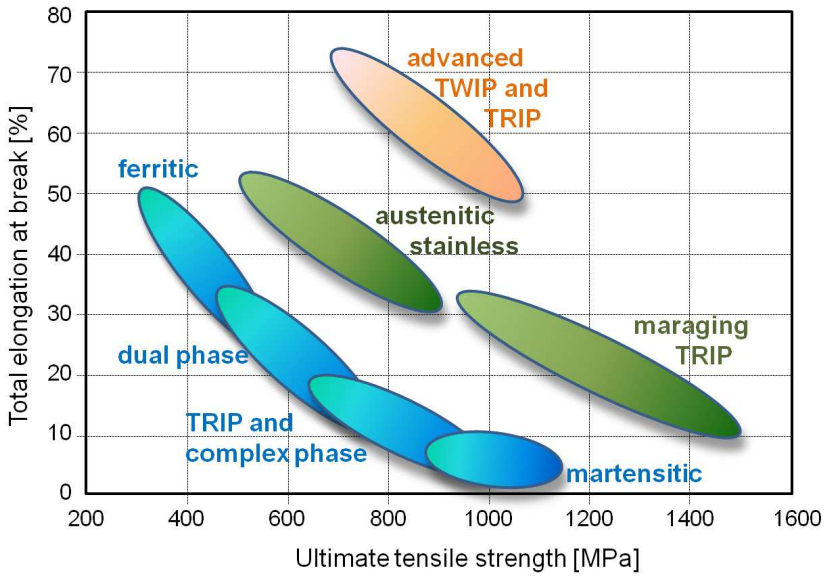

Figure 1: Overview of typical strength-ductility profiles of different types of steels, indicating an inverse relation between these two properties. Advanced steels showing transition/twinning induced plasticity (TRIP/TWIP) as well as novel concepts combining TRIP with the formation of intermetallic nanoparticles in the martensite during aging are most promising for applications. [1]

instance, steel sheets with a high ductility can be substantially deep drawn, which is necessary to construct complicated car elements. If at the same time a high strength level in particular for the deformed regions is ensured, the usage of thin steel sheets is possible. The consequence is a significant reduction of production costs and material, being important in particular for highly efficient, light-weight cars. Since the same material properties are also essential in case of crashes, the safety of a car will increase simultaneously. These extraordinary properties should go along with further constraints, such as good formability, excellent welding behaviour, and resistance to embrittlement, which every steel needs to fulfil.

The engineering task of exploring the materials landscape for such property combinations is also of high interest for natural scientists, since novel ways of materials design, rooted in fundamental scientific principles, are nowadays developed and employed to achieve the goal. All currently promising approaches try to design steels such that certain micro-structural elements and/or deformation mechanisms occur intentionally. Many of them are closely related to the thermodynamic (meta)stability of certain phases. Knowing the complex phase diagrams of these materials, certain annealing procedures can be designed to ensure the predominant occurrence of, e.g., martensite, austenite, or bainite. The solubility of alloying elements can lead to solid-solution hardening. Non-metallic inclusions such as carbides, nitrides, and oxides can in the form of precipitates significantly hinder the motion of dislocations, provided their formation is thermodynamically and/or kinetically feasible. The complexity of the involved phase diagrams becomes apparent by noting that already elementary iron can be observed in at least five different solid phases, including the ferritic (α, bcc), the austenitic (γ, fcc), and the ε phase (hcp), the latter being (meta)stable at (ambient) high pressures. All other alloying elements (a steel

is typically a system of more than 10 components) even lead to a substantial increase of the number of relevant structural as well as magnetic phases.

A potential approach to overcome the inverse strength-ductility relationship is the adoptive change of micro-structure in regions where the highest deformation rates occur. One of these mechanisms is the transition induced plasticity (TRIP), describing a local martensitic transformation of an austenitic (fcc) steel into a martensitic phase (hcp or bct). Another one is twinning induced plasticity (TWIP), resulting in the formation of $\Sigma_3[110](111)$ twin boundaries in an austenitic phase. Both processes allow large elongations without losing local strength by introducing stacking faults into the system. Therefore, the stacking fault energy (SFE), which can be related to the Gibbs free energies of the fcc and hcp phase of the steel, is typically used to predict their occurrence.

Most of the above mentioned properties can only be understood, if the processes on the atomic scale are fully taken into account. While empirical potentials are of importance in exploring possible physical mechanisms, they are not (yet) sufficient to yield a true predictive power for the complex processes in steels. This fact is mainly due to the occurrence of structures, not included in the fit of the potentials, due to the large variety of the involved elements and the complex magnetic degrees of freedom present in steels. Therefore, *ab initio* methods and most prominently density functional theory (DFT) seem to be best suited for state-of-the-art materials design.

There are however important challenges connected with such an approach that need to be carefully addressed. On the one hand, DFT is well known to be particularly suitable for ground state properties of materials. A ground state analysis is however not sufficient for steels which are processed at/for temperatures ranging from room temperature up to the melting point. An extension to finite temperatures is particularly evident for the presently hot topic of high-temperature applications as, e.g., urgently needed for next generation power plants.

On the other hand, current knowledge indicates that extreme demands with respect to the precision and accuracy of the methods need to be satisfied, in order to make truly profitable predictions in the field. It is for instance known from DFT calculations that magnetic phases of fcc iron while differing by only a few meV/atom can still significantly influence for example vacancy and other defect formation energies. CALPHAD assessments, an established phenomenological technique to construct phase diagrams from calorimetric measurements, predict the energy difference between fcc and bcc iron in the stability range of γ iron to be systematically below 1 meV/atom [2]. Further, it is empirically known that changes of the SFE by less than 10 $\mathrm{mJ/m^2}$ can have a noticeable influence on the kind of deformation mechanism (TRIP vs. TWIP) becoming active in austenitic steels [3, 4]. These accuracy demands distinguish steels from many other material classes such as oxides, conventional semiconductors, etc., where typical energy differences are in the order of 100 meV.

The aim of this article is to review the *ab initio* techniques currently available for predicting thermodynamic properties of materials and steels. Special care will be taken in covering the complete set of relevant excitation mechanisms at finite temperatures including - besides the "standard" vibrational and electronic excitations - in particular those related to the magnetic degrees of freedom. The achievable precision and the predictive power of these methods will

be discussed. Based on selected examples, distinguished success stories contributing to a true understanding of materials behaviour will be provided.

1.2 Established approaches of *ab initio* thermodynamics

The prediction of the thermodynamic stability of phases as a function of temperature and chemical composition is already for several decades a key task of the CALPHAD (abbr. for "Calculation of phase diagrams") community [5]. The tremendous success of this approach is due to sophisticated interpolation schemes, which allow the prediction of multi-component material systems based almost exclusively on input for unary, binary and ternary phases. A fundamental difficulty related to the typical CALPHAD approach is however the fact that it requires experimental input. Providing sufficient experimental data is often challenging and accompanied by expensive sample preparation and the necessity of high precision measurements. Further, from a principle point of view, some necessary input (e.g., energetics of metastable or even unstable phases) is missing due to the lack of corresponding samples.

The *ab initio* approach constitutes therefore a very promising possibility to explore experimentally inaccessible phase space regions and to evaluate existing experimental data [6]. It also provides a reference to evaluate the physical concepts that enter the interpolation formulas used in CALPHAD (e.g., with respect to stacking fault energies or magnetism).

There are already numerous examples in the literature [7, 8, 9, 10, 11, 12] where *ab initio* results have been used as an input for CALPHAD assessments. However, in almost all cases this combination is restricted to T=0 K values on the *ab initio* side and predominantly focusing on formation enthalpies of different phases. The restriction to T=0 K is not surprising recalling the ground state character of DFT. Knowing on the other hand that "standard" CALPHAD assessments fail to describe the temperature regime below 200 K due to missing experimental data, a fundamental gap between the two approaches becomes apparent. An extension of the *ab initio* approaches to finite temperatures is in this light a critical step towards a complete and fully predictive coupling between *ab initio* and CALPHAD. Specifically, this requires accurate yet numerically efficient theoretical approaches to compute all relevant free energy contributions such as harmonic and anharmonic atomic vibrations, electronic and magnetic excitations, or due to intrinsic point defects.

Some concepts for including finite temperatures into the *ab initio* description are already for quite some time on the market. One of these concepts addresses the inclusion of *electronic degrees of freedom*: In 1965 the "standard" T=0 K ground state DFT of Hohenberg and Kohn was extended to include electronic excitations within finite temperature DFT [13]. The method yields in principle (i.e., given the true exchange-correlation (xc) functional) the exact minimum of the full free energy surface. It is in this sense still a ground state approach, referring now, however, to the thermodynamic ground state at some given temperature rather than the T=0 K ground state. As a consequence, single particle (electron) excitations cannot be resolved within finite temperature DFT, but enter the electronic free energy in an averaged way. Furthermore, the fact that we do not know the exact xc-functional but have to rely on approximations also affects the accuracy with which we can compute this free energy contribution. Nonetheless, for weakly correlated materials this combination provides a straight forward and remarkably

accurate access to the electronic excitation processes and derived thermodynamic properties.

For alloys and solid solutions, which are often characterized by chemical disorder, i.e., disorder of the atomic species, highly advanced methods to treat *configurational entropy* are available. The thermodynamics of the disorder can be captured, e.g., with cluster variational methods [14] or Monte Carlo simulations based on cluster expansions [15]. Within the latter approach *ab initio* results of numerous crystal structures are used to parametrize a Hamiltonian, which mimics all kinds of atomic interactions. Cross-validation schemes are the key to check the numerical error related to the truncation of the Hamiltonian and to provide converged results. This approach has been extensively and highly successfully applied to predict binary and ternary phase diagrams and to study the formation of nano-sized precipitates.

Even the inclusion of *lattice vibrations*, yielding the largest entropy for pure or well ordered systems, is by now well established. Phonon calculations are most often performed in a harmonic approximation, using either supercell calculations where forces obtained from the Hellmann-Feynman [16, 17] theorem directly enter the dynamical matrix, or perturbative approaches in reciprocal space using linear response theory [18]. For complex systems both approaches yield phonon spectra of comparable precision and computational effort, two aspects which will be discussed in more detail in Sec. 2.1. Having obtained the phonon excitation energies, thermodynamic potentials like the Helmholtz free energy become directly accessible using statistical concepts:

$$F^{\mathrm{qh}}(V,T) = \frac{1}{3N}\sum_{i}^{3N-3}\left\{\frac{1}{2}\hbar\omega_i(V) + k_{\mathrm{B}}T\ln\left[1-\mathrm{e}^{-\hbar\omega_i(V)/k_{\mathrm{B}}T}\right]\right\}. \tag{1}$$

Here, N is the number of atoms in the supercell, ω_i are the phonon frequencies for each degree of freedom, k_{B} is the Boltzmann constant, $\hbar$ is the reduced Planck constant, V is the volume, and T the temperature.

In the next section we will give a brief overview on some recent methodological developments and advances to study further free energy contributions by DFT.

2 Recent methodological developments

One reason for the difficulties associated with thermodynamic *ab initio* predictions for steels is their complexity, both with respect to the involved phases and the relevant excitation mechanisms. In this article, we approach this challenge step by step. We first consider individual phases. Our primary focus is here on the fcc phase, which is of great relevance particularly for modern high-strength and stainless steels. Furthermore, we refrain in the first part from including configurational or magnetic degrees of freedom. Therefore, only non-magnetic, pure elements in the fcc structure will be considered. These conditions will be released as we proceed further.

2.1 Vibrational entropy beyond the harmonic approximation

As mentioned in the previous section, *ab initio* calculations of phonons in the harmonic approximation can nowadays be considered as a well established technique. However, to achieve

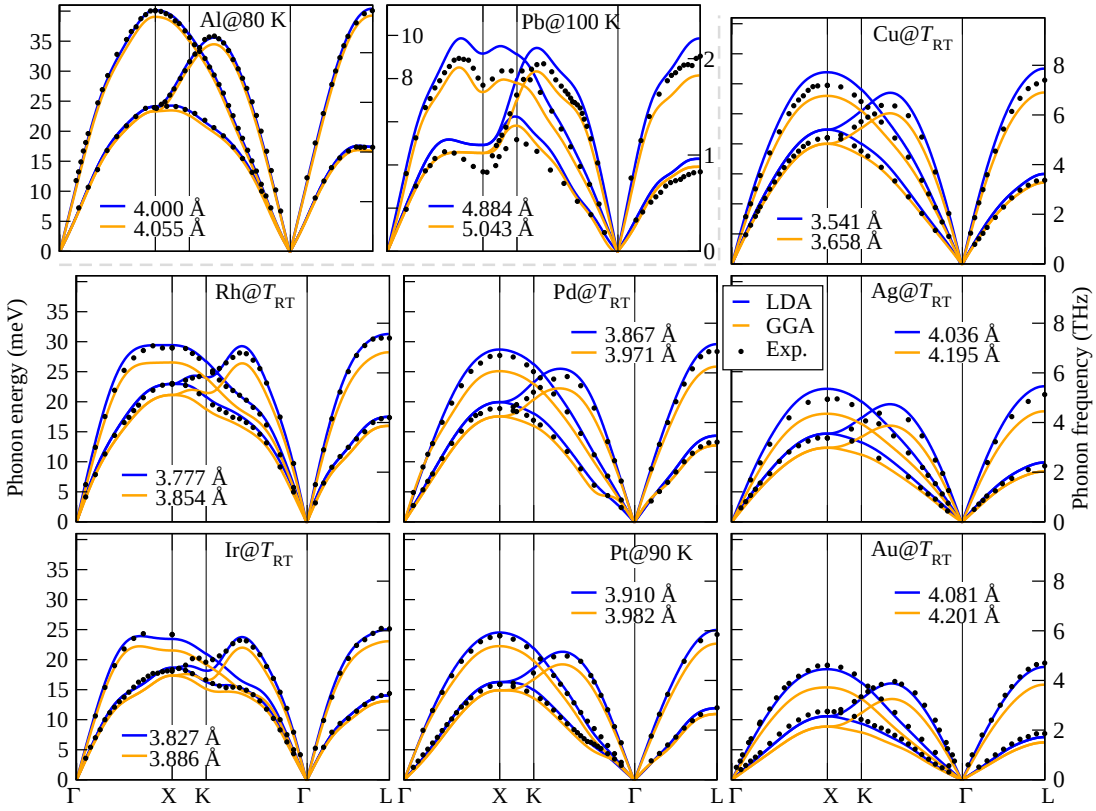

Figure 2: State-of-the-art performance of a DFT based quasiharmonic approximation to obtain phonon energies of non-mangnetic unary fcc metals. The legend shows the equilibrium lattice constant corresponding to the temperatures at which the dispersion was obtained and T_{RT} indicates room temperature. The calculations have been done using the VASP package [19] in combination with the provided PAW potentials [20]. The figure has been adapted from Ref. [21].

a precision in phonon energies sufficient for a reliable prediction of free energies, several crucial details have to be considered. Figure 2 shows the presently achievable accuracy when computing phonons using widely used xc-functionals (LDA, GGA-PBE) for a large set of non-magnetic fcc metals.

To achieve a fair comparison of the theoretical results with experiment, as done in Fig. 2, one needs to carefully revisit the origin of the corresponding data. Since experimental phonon measurements, usually obtained by neutron scattering experiments, are performed at finite temperatures, the temperature dependence of phonons needs also to be included in the theoretical calculations. In most practical cases the largest contribution arises from quasiharmonicity, as can be seen for the example for aluminium in Fig. 3. In this approximation the full volume dependence of the free energy surface is considered and all phonon calculations are performed for the lattice constant belonging to the respective temperature.

As shown in Fig. 3 the quasiharmonic approach does not cover the full anharmonicity of the problem. The interaction of phonons with other phonons (explicit anharmonicity), but also the coupling with other excitation mechanisms (e.g., with electronic or magnetic degrees of freedom) can lead not only to a broadening of the phonon peaks, but also to a shift of their

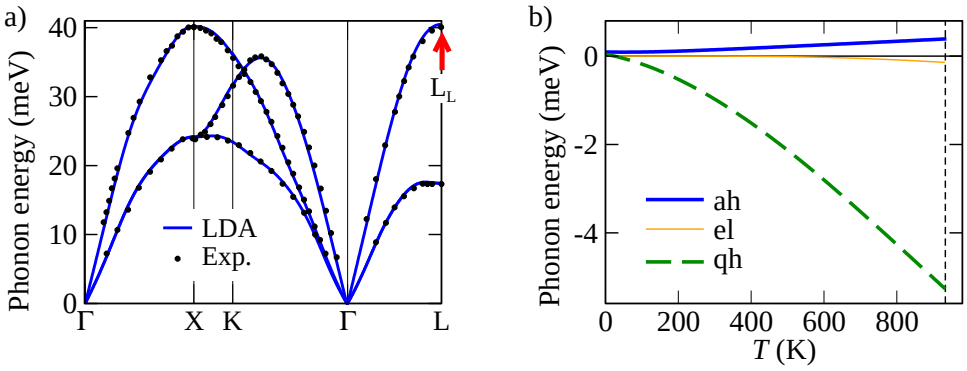

Figure 3: Influence of temperature on phonons. a) Phonon dispersion of aluminium at 80 K as in Fig. 2. b) Comparison between the various temperature dependencies of the phonon frequency at the L_L point (indicated by a red arrow in a)): the explicitly anharmonic (ah) shift (see text), the shift due to electronic (el) excitations, and the shift due to quasiharmonicity (qh), i.e., influence of thermal expansion [22].

maxima. Whereas explicit anharmonicities usually impact thermodynamic data particularly at high temperatures, the influence of non-adiabatic interactions is very much system dependent. A few examples of this currently intensively investigated topic [23] will be mentioned below, several others can be found in the literature, e.g. [24].

In order to ensure a high numerical precision when computing the various free energy contributions, great care needs to be taken to sufficiently converge the results. Since a large number of parameters needs to be optimized, efficient scaling procedures can be applied for this purpose [21]. Some of the most important aspects for phonon calculations are:

- For some elements (e.g., Cu) the grid size of the augmentation charges needs to be increased well beyond standard values in order to obtain a convergence of the Grüneisen parameter to less than 1%.
- For some elements (e.g., Al) extraordinary high k-point meshes for the electronic integration are necessary. Inappropriate k-point meshes can even yield unphysical imaginary phonons in the vicinity of the Γ point.
- In the direct force-constant method the supercell size is a critical parameter. In order to resolve the phonon dispersion with sufficiently high precision (e.g., Pb) or to identify small (Kohn) anomalies in the phonon spectra (e.g., Pt), the supercell size needs to be sufficiently large.

A high precision enforced in the phonon calculations allows us to unambiguously assign the remaining errors to (i) missing free energy contributions such as non-adiabatic contributions mentioned before and (ii) the xc-functionals providing unique information regarding sources of their failing. Figure 2 shows that LDA overestimates the experimental data in most cases, while GGA underestimates it. This behaviour is surprisingly systematic [21] and consistent with the performance of these functionals already at T=0 K (see Fig. 4): The overbinding of LDA and the corresponding too small lattice constant leads to a prediction of a stiffer material with

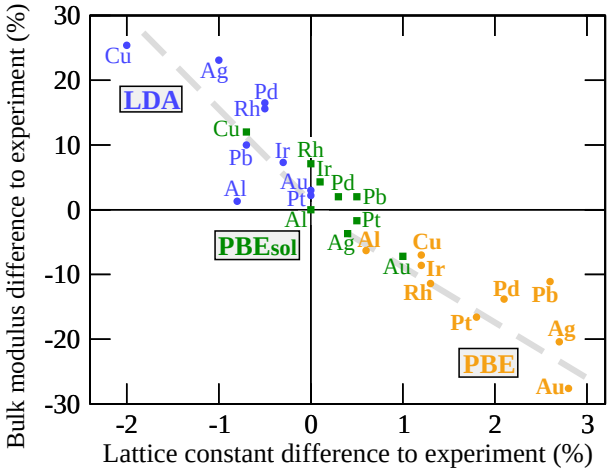

Figure 4: Correlation between the deviation from experiment for the lattice constants and the bulk moduli. The results for the three different exchange-correlation functionals LDA, GGA-PBE, and GGA-PBEsol are shown in blue, orange, and green, respectively.

a bulk modulus which is too large as compared to experiments. The opposite correlation is observed for GGA. The situation cannot simply be resolved by using the experimental value for the lattice constant, since this results into an artificial inner pressure of the system. Even if the same (experimental) lattice constant is used for both xc-functionals, the corresponding difference in phonon energies remains almost the same and only their order is reversed, i.e., LDA/GGA under/overestimates the experimental phonons, respectively. The only way out of this dilemma is the development of improved xc-functionals. As can be seen in Fig. 4, PBEsol [25] is significantly reducing the over-/underbinding of LDA/GGA for non-magnetic metals. Since PBEsol, however, does not improve the description of magnetic materials, which are the main objective of this paper, we will not consider this xc-functional in upcoming discussions.

The systematic behaviour of the xc-functionals becomes even more apparent in the heat capacities. They are obtained from a second derivative of the free energy (calculated with Eq. (1)), which is most often the target quantity for materials research. The heat capacity, however, provides a more sensitive response to even tiny errors in the free energy. We learn from Fig. 5 that the consideration of more than one functional yields an ab initio confidence interval in the following sense: Whenever the derived thermodynamic quantities are largely independent of the chosen xc-functional, a high predictive power, i.e. agreement with (unknown) experiments, can be expected. If, however, a large deviation between LDA and GGA is observed, one has to assume theoretical error bars of approximately the same order of magnitude. This observation does not significantly change, if instead of the self-consistent lattice parameters, the lattice constant for both xc-functionals is fixed to the experimental values.

The large amount of chemical elements considered here, allows to derive chemical trends for the accuracy of the DFT computed thermodynamic data. We first note that with the filling of the *d*-shells (from left to right in Fig. 5) the deviation from the experiments becomes larger. Furthermore, an increase of the size of the considered atoms (from top down in Fig. 5) gives also a larger scatter in the theoretical data. In particular for the noble metals Ag and Au, we

attribute this effect to Van de Waals interactions, not considered in our approach.

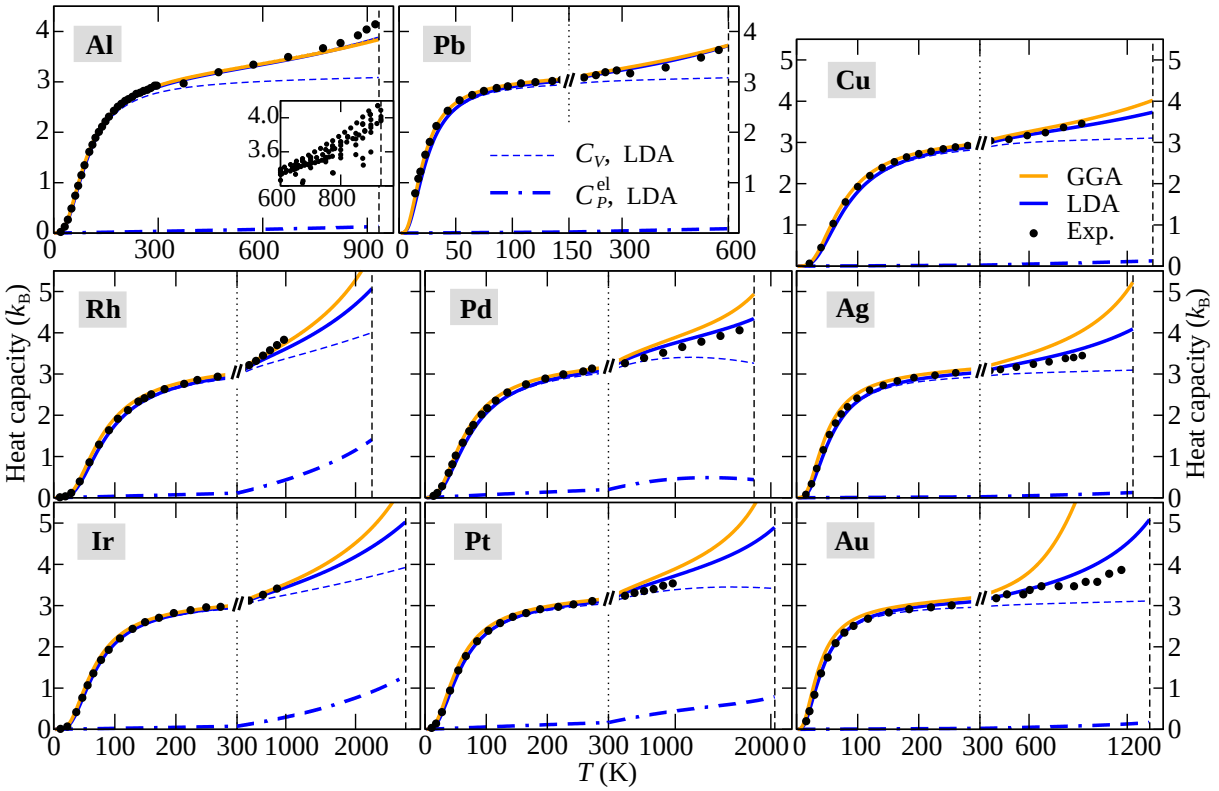

Figure 5: Isobaric heat capacity C_P as a function of temperature T for a variety of fcc metals, as obtained from a quasiharmonic approximation using only DFT results as input. The contribution due to electronic excitations C_P^{el} as well as the constant volume heat capacity C_V are also included. The results are obtained at P=0 Pa and are provided in units of the Boltzmann constant k_{B}. The temperature axis is split by the vertical dotted line into two parts to allow a convenient representation. The melting temperature is indicated for each element by the vertical dashed line. The experimental data are taken from Ref. [26].

The results shown in Fig. 5 contain in addition to the lattice vibrations also contributions due to electronic excitations. The relevance of this entropy contribution depends strongly on the specific chemical element. The electronic entropy contribution is particularly large for transition metals with an almost half filled d-shell. For example, fcc Rh shows a prominent peak in the density of states close to the Fermi energy, which only at finite temperatures becomes partially occupied.

Since the electronic contribution to the heat capacity is surprisingly large for elements such as Rh, the question immediately occurs, what the effect of a finite electronic temperature on the phonon energies is. This effect has systematically been studied in Ref. [22] and the result for Al is shown in Fig. 3. The resulting corrections for the heat capacity, shown in Fig. 6, are even for Rh one order of magnitude smaller than the electronic correction itself, and therefore in most cases expected to be not significant in computing thermodynamic properties relevant for materials design.

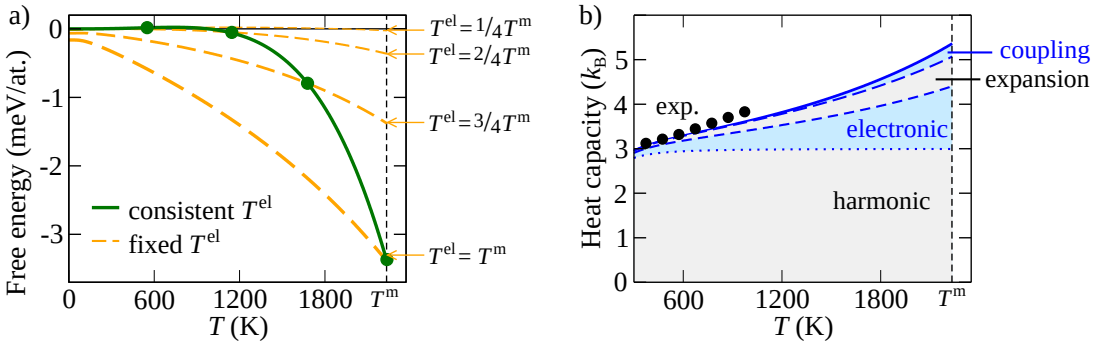

Figure 6: Illustration of the influence of the phonon shift due to a finite electronic temperature on the thermodynamic properties of Rh. For this purpose the quasiharmonic free energy has been calculated for various electronic temperatures, T^{el} (relative to the melting temperature T^m), and an appropriate interpolation scheme has been applied (a). The individual harmonic, electronic, quasiharmonic (expansion) and (quasiharmonic-electronic) coupling contributions to the heat capacity are displayed (b).

2.2 Explicit anharmonicity

Explicit anharmonicity, while on an absolute scale significantly smaller than the quasiharmonic contribution, often dramatically changes around phase transitions, e.g., close to the melting temperature or to martensitic transitions. In contrast to the quasiharmonic free energy contribution described above very few *ab initio* studies to compute anharmonic free energy contributions of metals and metallic alloys have been reported so far. This is largely related to the fact that an accurate determination of anharmonicity requires a well converged sampling of the full $3N$-dimensional configuration space (with N the number of atoms in a supercell) whereas for the harmonic contribution at most $3N$ *configurations* need to be sampled. The number of configurations can be reduced even further when considering single crystals where translational and point group symmetries can be employed.

To address the above challenge of sampling a high dimensional configuration space various approaches have been proposed. These approaches can be divided into three major classes: (i) Explicit calculation of third and fourth order force constant tensors, (ii) molecular dynamics in connection with temperature integration, and (iii) adiabatic coupling approaches calculating only the difference between a reference system, where the free energy can be easily computed, and the actual system. Each of these approaches has its pros and cons. While (i) is a natural extension of the dynamical matrix, it becomes highly memory and time consuming for low symmetry structures such as disordered metallic alloys. Using empirical potentials, approach (ii) has been employed to compute the anharmonicity of metals, e.g., [27]. However, to obtain a statistical convergence of ≈ 1 meV in the free energy about $10^6 \ldots 10^7$ atomic configurations have to be computed making this approach infeasible for DFT calculations. Approaches based on (iii) rely on reference systems where the free energy can be analytically computed (e.g., in the harmonic approximation, see Sec. 1.2) and for which the energy difference between the full and the reference free energy surface is close to a constant. Using efficient adiabatic connection schemes such as thermodynamic integration the number of configurations can be reduced by a factor of $10^2 \ldots 10^3$.

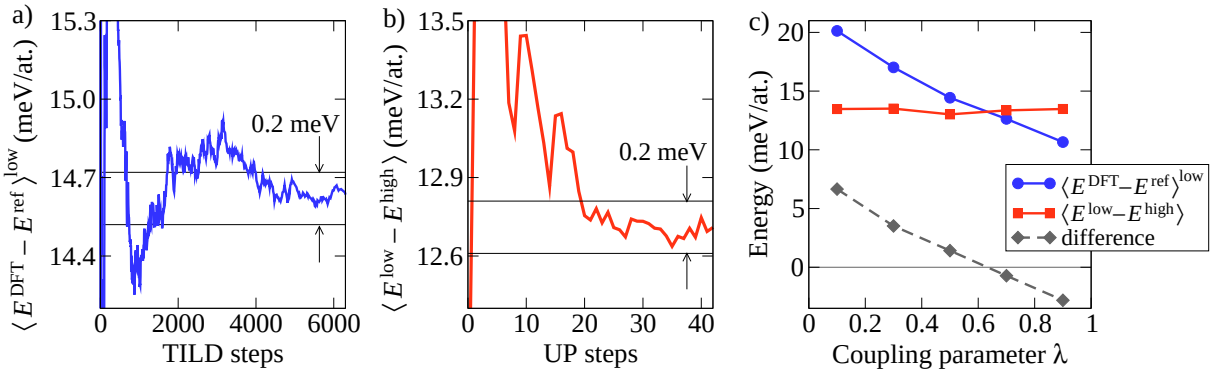

Figure 7: Illustration of the UP-TILD method for Al. a) Convergence for a "usual" thermodynamic integration run ($V = 15.7\mathring{A}^3$, T=900 K, and λ=0.5) performed with low converged parameters. b) Convergence of the average energy difference $\langle E^{\text{low}} - E^{\text{high}} \rangle$ for a set of uncorrelated MD structures taken from the run in a). c) The λ dependence of the converged quantities from a) and b) and their difference are shown. The calculations have been performed with the Sphinx software package [30].

This approach has been successfully employed to determine, e.g., the solid/liquid phase transition of iron (at extreme pressures) by computing the free energy difference between the solid and liquid state using DFT [28].

While thermodynamic integration substantially reduces the number of configurations needed to sample the 3N configuration space the targeted accuracy of 1 meV requires convergence parameters which make the sampling of 10^4 configurations for a single free energy point infeasible. By systematically studying the performance of the various approaches it is possible to design a multi-step approach [29] that provides the targeted accuracy within a few 100 steps only, i.e., providing a speed up compared to thermodynamic integration of 100 and to conventional MD of more than 10000. The approach is based on the observation that the extreme high convergence parameters in k-point sampling and energy cut-off are mainly needed to converge the kinetic electronic energy, while the charge density is well described already at significantly reduced convergence parameters. Thus, increasing convergence gives rise to a substantial volume dependent shift in the energies but affects the forces and thus the shape of the potential energy surface only little. As a consequence we observe that energy differences between medium and high converged calculations for identical configurations are almost constant. This is shown by the red line in Fig. 7c.

This insight allows, as mentioned above, to efficiently coarse grain configuration space without having to sacrifice accuracy. In a first step, starting from a harmonic reference potential energy surface (PES)

$$E^{\text{ref}} = \sum_{i,j} \mathbf{u}_i D_{i,j} \mathbf{u}_j, \tag{2}$$

with the dynamical matrix D, displacements $\mathbf{u}_i = \mathbf{R}_i - \mathbf{R}_\mathbf{i}^\mathbf{0}$ and $\mathbf{R}_\mathbf{i}^\mathbf{0}$ the T=0 K equilibrium position, a thermodynamic integration for medium convergence parameters is performed. For

this subsequent MD runs on the PES

$$E^{\lambda} = E^{\mathrm{ref}} + \lambda \cdot \left(E^{\mathrm{DFT}} - E^{\mathrm{ref}} \right) \tag{3}$$

are performed with λ an adiabatic coupling parameter going from 0 to 1. A critical aspect to achieve maximum efficiency in these calculations is the choice of the thermostat and of the initial conditions (coordinates and velocities at time t=0). Rather than using the conventionally often employed Nose-Hoover thermostat we use Langevin dynamics. Particularly for small λ values, where the PES is close to the harmonic regime phonon-phonon interactions are weak resulting in huge equilibration times when using conventional thermostats. In contrast, Langevin dynamics rapidly equilibrates even in a fully harmonic potential making it an optimum choice in connection with thermodynamic integration. As initial configurations snapshots of equilibrated MD runs on the reference PES, Eq. (2), are used. Based on these choices 10 equally spaced λ values and 1000 MD steps (i.e. a total of 10000 configurations) provide a statistical convergence of better than 1 meV.

In a second step we collect from each λ trajectory 30-50 uncorrelated configurations and perform for these structures DFT calculations with the highest convergence. As shown in Fig. 7b the small number of steps is sufficient to guarantee the targeted accuracy. Based on the key ingredients which guarantee the high efficiency this approach has been named UP-TILD (upsampled thermodynamic integration using Langevin dynamics).

A major advantage of the UP-TILD approach is that it provides an optimal minimal set of configurations that highly efficiently samples each of the PES given by Eq. (3). The compact notation of the high dimensional configuration space easily allows to bridge not only medium with high converged DFT calculations but also different *ab initio* approaches. We have used it, e.g., to construct minimal sets in a pseudo-potential approach and transferred it to all electron calculations employing WIEN2k [31] to eliminate potential inaccuracies due to the pseudo-potentials. This ensures that indeed only the xc functional remains as only non-controllable parameters that defies the targeted 1 meV accuracy. Since only configurations but no forces are needed for the upscaling advanced electronic structure methods going beyond DFT such as quantum Monte Carlo (QMC) can be easily employed.

2.3 Free energy contribution due to point defects

Among all possible defects occurring in technical metallic alloys such as dislocations, grain boundaries, voids, etc. only point defects have a sizeable configurational entropy and may thus contribute to the free energy. The free energy due to the formation of native point defects is a sum of different contributions (e.g., vacancy, interstitial, anti-site), where the equilibrium concentration of the specific defect is given by $c_i = c_0 \exp(-F_i/k_B T)$. Here, c_0 is the concentration of available sites where the specific defect can be formed. The key quantity to determine the free energy contribution is the volume and temperature dependent formation free energy F_i. From a DFT perspective there are two major challenges to compute this quantity:

1. Finite temperature contributions
2. Finite supercell size effects

Let us first focus on the finite temperature aspect. The dominant contribution to F_i is the zero temperature formation energy E_i, which can be nowadays obtained at modest computational cost. Despite the fact that E_i is the T=0 K formation energy it leads to temperature dependent defect properties – such as concentrations – due to the temperature dependence of the *configurational defect entropy*. However, for the targeted accuracy of 1 meV in the defect related free energy contribution – similar as for bulk thermodynamic quantities – also second order contributions such as electronic, quasiharmonic, and anharmonic excitations need to be included. The loss of translational symmetry and the reduced point group symmetry induced by point defects make a DFT calculation specifically of the quasiharmonic contribution much more challenging.

In order to address these challenges and to push the accuracy and realism of the defect calculations numerous approaches have been developed in the past. In this respect, it is instructive to look at the methodological developments over the last 25 years for the example of the dominant point defect in metals – the vacancy (Tab. 1): Starting in the late 80's with the seminal work by Gillan [32], DFT based studies of point defects were limited to E^{f}. This situation persisted roughly until the beginning of the new century, when studies [33, 34] of the electronic contribution to F^{f} – which are as discussed in Sec. 2.1 of crucial importance for some metallic materials – appeared. In 2000 and 2003, Carling et al. [35, 36] provided a first *ab initio* based assessment of the quasiharmonic contribution to the vacancy of aluminum. To make such a study feasible at that time, the authors had to restrict the dynamics of the system to the first shell around the vacancy, i.e., to the atomic shell which experiences the largest effect as compared to the perfect bulk. An *ab initio* based evaluation of the anharmonic contribution was computationally prohibitive at that time, which made it necessary to resort to empirical potentials.

Today, major methodological improvements and the boost in computer power provide the unique opportunity to study all relevant free energy contributions of defect formation in a rigorous *ab initio* manner (cf. Tab. 1). To actually perform such a study required developing and implementing new concepts. For example, the fact that even small deviations in the treatment of bulk and defect calculations lead to unacceptable errors in the targeted accuracy enforce great care and specific modifications, e.g., in the quasiharmonic treatment [37].

To briefly discuss key aspects of some of the new approaches and to demonstrate their capabilities we discuss in the following an exemplary point defect: The vacancy defect in bulk Al. For this material systematic experimentally measured vacancy concentrations over a large temperature range are available allowing a direct comparison with our DFT data.

To achieve the targeted accuracy in the free energy a correct treatment of strain induced finite size effects due to periodic boundary conditions is crucial. Without these, errors of more than one order of magnitude in the defect concentration are observed (see e.g., [29]). To eliminate the artificial defect-defect interaction two major approaches are used: The constant pressure approach [39] and the rescaled volume approach [32]. The approaches differ in how they account for the long-ranged elastic interactions. Recently, a volume optimized approach [29, 37] has been developed which is more general and allows to derive the other two by well defined approximations.

Table 1: Representative *ab initio* studies of point defect calculations in unary metals for the specific case of vacancies. The abbreviations are: 3d/4d/5d = respective transition elements, xc = exchange-correlation functional, LDA = local density approximation, GGA = generalized gradient approximation, PWps = planewaves with pseudopotentials, FP-LMTO = full potential linearized muffin tin orbitals, PW-PAW = planewaves with projector augmented waves [38], V = rescaled volume approach [32], P = constant pressure approach [39], volOpt = volume optimized approach [37], F^{f} = defect formation free energy, $E^{\mathrm{f}} = (T = 0\,\mathrm{K})$ contribution to F^{f}, el/qh/ah = electronic/quasiharmonic/anharmonic contribution to F^{f}, 1s = first shell (around the defect) contribution to the dynamical matrix, emp = empirical potential approach.

			Methodology			Contributions to F^{f}			
Year	Ref.	Elements	xc	Potential	Strain	E^{f}	el	qh	ah
1989	[32]	Al	LDA	PWps	V	**x**			
1991	[40]	Li	LDA	PWps	V	**x**			
1993	[41]	Al,Cu,Ag,Rh	LDA	FP-LMTO	V	**x**			
1995	[42]	3d,4d,5d	LDA	FP-LMTO	V	**x**			
1997	[39]	Al	LDA	PWps	P	**x**			
1998	[33]	W	LDA	PWps	P	**x**	**x**		
1999	[34]	Ta	LDA	PWps	P	**x**	**x**		
2000	[35]	Al	LDA/GGA	PWps	P	**x**		$\mathbf{x}^{\mathrm{1s}}$	$\mathbf{x}^{\mathrm{emp}}$
2003	[36]	Al	LDA/GGA	PWps	P	**x**		$\mathbf{x}^{\mathrm{1s}}$	$\mathbf{x}^{\mathrm{emp}}$
2009	[43]	Fe	GGA	PW-PAW	V	**x**		**x**	
2009	[29]	Al	LDA/GGA	PWps/PW-PAW	volOpt/P	**x**	**x**	**x**	**x**

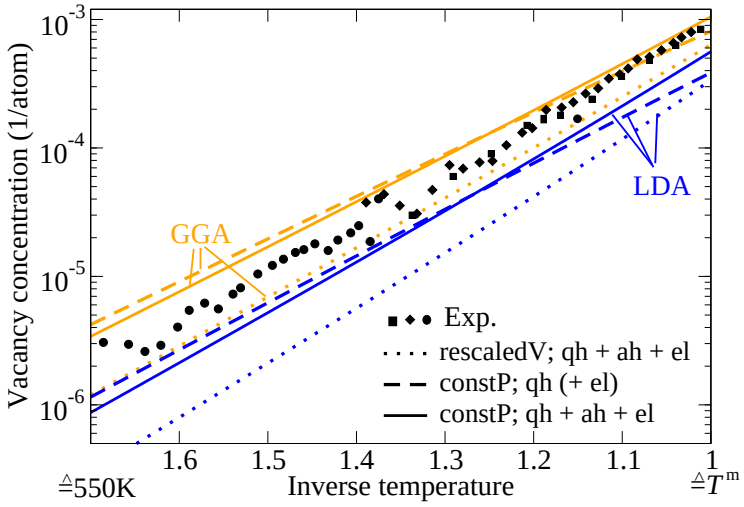

Figure 8: Equilibrium vacancy concentration at zero pressure of aluminium as a function of the inverse temperature multiplied by the melting temperature T^{m}. Results for the rescaled volume and constant pressure approach are shown. The volume optimized approach yields concentrations which are identical to the constant pressure results on the shown scale. The electronic contribution yields a negligible contribution (indicated by the parenthesis). The squares indicate experimental values from Ref. [44] (differential dilatometry). The diamonds/circles indicate experimental values from Ref. [45] (differential dilatometry/positron annihilation).

A main feature of the optimized volume approach is a concentration dependence of F^{f} which enters through the reduced (excess) volume induced by atomic relaxations around the defect and which is not present in the two previous approaches. While the volume optimized approach allows to naturally derive both, the constant volume and pressure approximation, extensive tests showed that in relevant defect concentration ranges the extra term is small resulting in defect formation energies almost identical to the constant pressure approach [37]. In contrast, the approximations needed to derive the rescaled volume approach are more severe for realistic supercell sizes and result in sizeable errors even for low defect concentrations (see also Fig. 8).

Figure 8 shows also that including all entropy contributions (excitation mechanisms) together with a high control in numerical precision provides an amazing accuracy using conventional LDA or GGA functionals. Similar like for other thermodynamic quantities we observe that LDA and GGA provide approximate theoretical error bars with LDA/GGA giving an lower/upper bound to the experimental data. While including the anharmonic contributions has little influence on the absolute defect concentrations in the experimentally available temperature window a more detailed analysis performed in [29] shows a large change: While neglecting the quasiharmonic approximation results almost in a vanishing vibrational entropy (0.2 k_B) including these contributions gives an entropy of 2.2 k_B very close to the experimentally derived one (2.4 k_B).

The excellent agreement of DFT computed and actually observed defect concentrations indicates that the associated free energy bulk contribution can be accurately predicted.

2.4 Magnetic entropy

For metallic alloys with strong local magnetic moments such as steels the above mentioned contributions to the free energy are not sufficient for a complete description of thermodynamic properties. One observes, e.g., in the heat capacity plot for bcc iron in Fig. 9 an enormous discrepancy between the calorimetric measurements (open circles) and *ab initio* results that consider only vibrational and electronic entropy contributions (orange line). The latter agrees with the experimental data only up to room temperature, which is also found in Ref. [46]. At higher temperatures, however, it cannot account for the rapid increase in the experimental heat capacity, having its maximum at the Curie temperature. This discrepancy has its origin already in the free energy when including only $F^{\mathrm{vib}} + F^{\mathrm{el}}$, showing an increasing deviation from the full CALPHAD values with temperature. For instance, at 1200 K, corresponding to the experimental bcc to fcc transition temperature, the difference is 45 meV – too high for a reliable description of thermodynamic properties of steels. It is, therefore, obvious that an accurate determination of the free-energy contribution from magnetic excitations is crucial.

Currently the entropy due to magnetic excitations cannot directly be determined within DFT. One approach is to use the GW approximation in order to solve the many-body problem of spin excitation in the electronic system [47]. This approach, which accounts for the itinerant nature of magnetism, has been particularly successful in simulating spectral properties such as magnon dispersion and life times. However, due to its methodological and computational complexity free energy calculations based on this approach have not been possible yet.

For iron and its alloys, the assumption of a localized magnetic model has often turned out to work surprisingly well. Based on this assumption a description of the magnetic entropy is typically obtained using a two step procedure. In a first step, the interaction of the localized magnetic moments is captured by a magnetic model Hamiltonian, the parameters of which are determined by DFT calculations. In a second step, the magnetic Hamiltonian is solved in order to derive the desired thermodynamic potentials.

The most established magnetic Hamiltonian for bcc iron is the Heisenberg model:

$$H = -\sum_{ij} J_{ij} \mathbf{S}_i \mathbf{S}_j. \tag{4}$$

It is entirely determined by the spin quantum number S and the coefficients J_{ij}, which describe the magnetic exchange coupling between magnetic moments at atomic sites i and j. S is formally connected to the local magnetic moment M_0 by $M_0 = g\mu_{\mathrm{B}} S$, with the Landé factor $g \approx 2$ and the Bohr magneton μ_{B}. For bcc iron, M_0 is almost entirely determined by the strongly localized $3d$ electrons, resulting in $S \approx 1.1$.

For extracting the magnetic exchange coefficients J_{ij}, we find the frozen magnon approach [48] in combination with employing the generalized Bloch theorem [49] to be highly efficient. In this approach, the DFT energy difference between spin spirals is calculated in reciprocal space. A major advantage of this approach as compared, e.g., to a derivation of J_{ij} from ordered magnetic configurations, is that it naturally accounts for non-collinear spins and long-range interactions. Not only are spin spirals with $\mathbf{q}$ vectors close to the Γ point due to their low energy most relevant for the thermodynamics. They are also most consistent with the assumption of a fixed

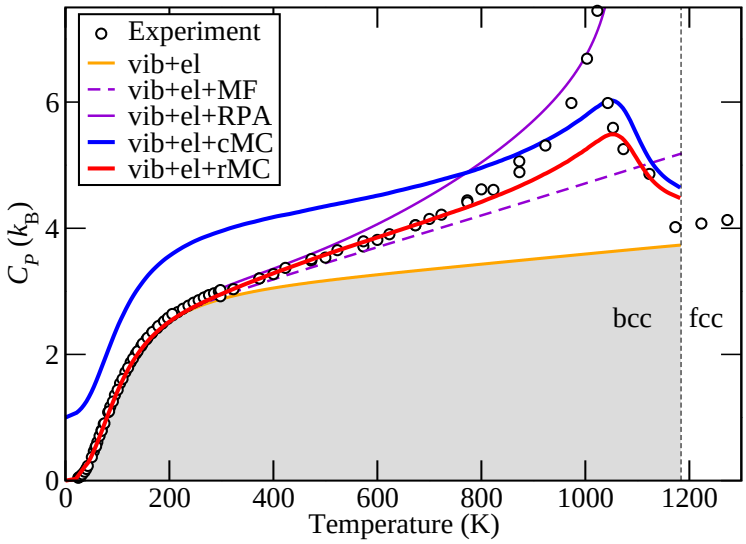

Figure 9: Heat capacity vs temperature of bcc Fe. The results of various theoretical methods (MF, RPA, cMC and rMC) explained in the text are shown. The experimental data (open circles) are taken from Refs. [51, 52] and the experimental transition temperature (bcc → fcc) $T^{\alpha\gamma} \approx 1184$ K is indicated by a dashed line. All cMC and QMC calculations were performed using the ALPS code [53].

spin quantum numbers S throughout the calculations. It is therefore not surprising that an almost perfect agreement of the calculated magnon spectra with low-lying experimental data (below the onset of Stoner excitations) is observed [50].

In the past various approaches to solve the Heisenberg model at finite temperatures have been developed. These can be roughly divided in the following categories: (i) analytic and (ii) numerical approaches. Another major distinction is with respect to treating spin, i.e. whether spin quantization is taken into account or whether the spin degrees are assumed to be classical continuous variables. Since the critical magnetic temperature of many magnetic metals such as, e.g., Fe, Ni, Co is well above room temperature spin quantization effects are commonly assumed to be negligible. Fig. 9 provides a first overview about the performance of the various approaches. Let us first focus on the analytical approaches where the inclusion of spin quantization is straightforward. The methodologically most approximate approach, the simple mean-field (MF) solution, does little to improve the heat capacity [50]. Higher order correlation functions can be included using the random phase approximation (RPA) [54]. Including these effects allows not only an almost perfect prediction of the Curie temperature, but also of the heat capacity up to the critical temperature [50]. However, above the Curie temperature by construction the method yields a vanishing magnetic entropy, i.e., the effect of local order cannot be captured.

To include local order effects in the paramagnetic temperature regime Monte-Carlo approaches are the method of choice. Neglecting spin-quantization effects, efficient classical Monte-Carlo (cMC) techniques can be used to solve the Heisenberg model numerically exact. As can be seen in Fig. 9 using this approach provides a correct description of the short range order effects in the paramagnetic region, i.e., a largely improved description above T_C. For temperatures below T_C,

however, even qualitative changes are observed (e.g., the incorrect scaling at T=0 K) making this approach unsuitable for a thermodynamic description over the entire temperature regime. The good agreement between the approximate analytical solutions (which fully include spin quantization) and experiment clearly indicate that spin quantum effects are critical and need to be included. To include spin quantization, the proper approach would be spin quantum Monte Carlo (QMC) [55, 56]. It provides a numerically exact solution of the quantum-mechanical Heisenberg model. While this approach has been highly popular and successful solving a wide range of model spin Hamiltonians, an application on actual magnetic metals turns out to be not feasible with the presently available numerical implementations. The reason is that the present implementations suffer from the so-called (negative) sign problem [57, 58], which results in an exponential increase of the statistical error if magnetic frustration is present. Since realistic metals are characterized by long-ranged oscillatory, i.e., positive as well as negative exchange integrals, giving rise to magnetic frustrated configurations in the statistical ensemble, a complete QMC solution of Eq. (4) is not feasible. For example, to obtain the desired accuracy for bcc iron magnetic interactions for more than 20 neighbour shells had to be included. The above discussion implies a severe discrepancy between the methods in principle needed to describe finite temperature magnetism and the magnetic interactions of actual materials. To resolve this discrepancy we systematically explored a wide range of pragmatic yet well defined approaches to make QMC applicable for magnetism in real metals. In the following two approaches will be discussed. To introduce the first one, we analyse the ratio between classical and quantum MC calculations of the heat capacity:

$$f(t, S, \sigma) := C_V^{\mathrm{QMC}}(t, S, \sigma)/C_V^{\mathrm{QMC}}(t, S, \sigma). \tag{5}$$

Here, σ labels the specific magnetic configuration, and $t = T/T_C$ is the normalized temperature. Choosing an extensive set of lattice structures (sc, bcc, and fcc) with nearest and second nearest-neighbour ferromagnetic ($J > 0$) as well as anti-ferromagnetic configurations ($J < 0$) a remarkable insensitivity of the scaling relation Eq. (5) with respect to the specific configuration, i.e., the choice of lattice or the interaction parameters is observed [59]. An example is shown in Fig. 10 for two different spins, $S = 1$ and $S = 7/2$. For high temperatures, where the quantum and classical solution should coincide, $f(t \gg 1) \to 1$, the data is noisy due to $C_V(t \gg 1) \to 0$ and the connected increase in the statistical errors. However, for the more important regime below $t = 1$, i.e., the regime where classical MC fails, the influence of σ on the scaling relation f is weak as discussed above and significantly smaller as compared to that of S and t.

The (approximate) independence of the scaling relation on crystallographic structure and magnetic interactions provides an elegant and direct way to combine the advantages of classical and quantum MC without being restricted by their respective limitations: Using the known scaling relation the magnetic Hamiltonian can be solved numerically exact for long range and oscillating magnetic interactions of realistic metals and transferred to their respective (approximate) quantum-mechanical result. For practical reasons it is convenient to parametrize $f(t, S, \sigma)$ by the function:

$$\bar{f}(t, S) := \left(\frac{2t_S/t}{\exp(t_S/t) - \exp(-t_S/t)} \right)^2. \tag{6}$$

The choice of this analytical function is motivated by limiting cases for t [59]. Interestingly, the only free parameter t_S in this function shows a linear dependence on the spin quantum number S

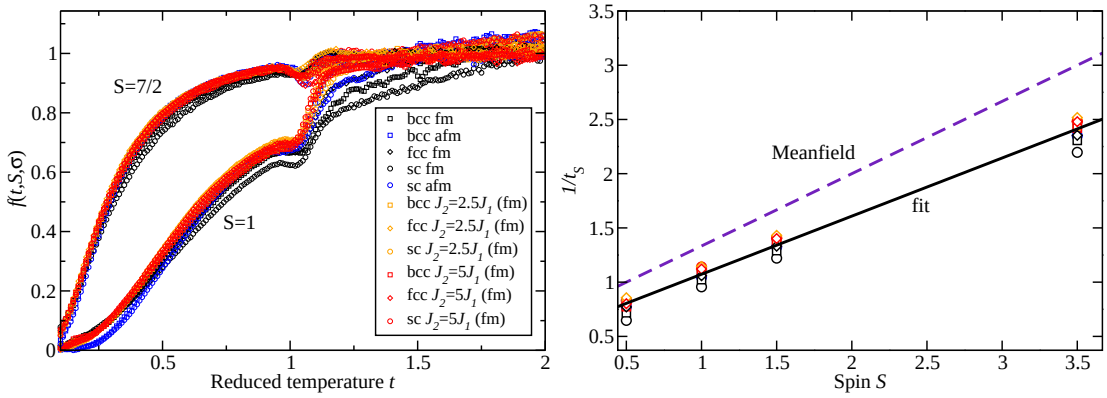

Figure 10: Numerically evaluated ratio of the heat capacity obtained from classical vs. quantum MC simulations, $f(t, S, \sigma)$ as a function of reduced temperature for two spins S=1 and S=7/2 and various lattice/magnetic configurations σ. The figures have been adopted from Ref. [59].

(see Fig. 10b)), which underlines together with the weak σ dependence in Fig. 10a the universal character of this behaviour.

With this insight, a fully quantum-mechanical treatment of bcc iron becomes accessible: Using the complete set of previously determined exchange integrals, the magnetic part of the heat capacity has first be determined within a classical MC simulation. Subsequently, Eqs. (5) and (6) have been used to obtain the quantum-mechanical correction. The result is plotted in Fig. 9, showing a remarkable agreement with experimental heat capacity data, both below and above the paramagnetic transition temperature.

The finding of an universal scaling relation was also the main motivation for a second approach to compute magnetic free energies with QMC [60]. Here one makes use of the observation that the specific magnetic configuration, i.e., the number of interaction shells and the magnetic order, has only a weak influence on the shape of C_p. Thus, rather than using the full, i.e. magnetically long range Hamiltonian, any Hamiltonian reproducing the shape and critical magnetic temperature of the heat capacity can be used. In case of a ferromagnetic solution, the numerically most efficient one is an effective nearest-neighbour spin Hamiltonian, which, however, keeps the crystal structure and spin quantum number of the investigated material. This construction guarantees that the negative sign problem does not occur. The effective exchange integral is then determined by the critical magnetic temperature, T_C, which remains to be the only input needed for this approach. It can be obtained from the full magnetic Hamiltonian using RPA, classical MC, or experimental measurements. [50, 61, 59]

The quality of the approach can best be seen, when deriving the magnetization curves for often-studied magnetic benchmark systems (Fe, Co, and Ni). Figure 11 reveals an excellent agreement with the highly accurate experimental data available for these materials. As indicated in the figure, the quantum-mechanical corrections as compared to a cMC simulation are essential and well captured by the nearest-neighbour QMC approach suggested here. One should also note that recently the calculation of magnetic properties of Fe and Ni with dynamical mean field theory (DMFT) became possible and provided a similarly good agreement with experiment [62]. The numerical effort behind these methods is, however, much higher. It is also important to

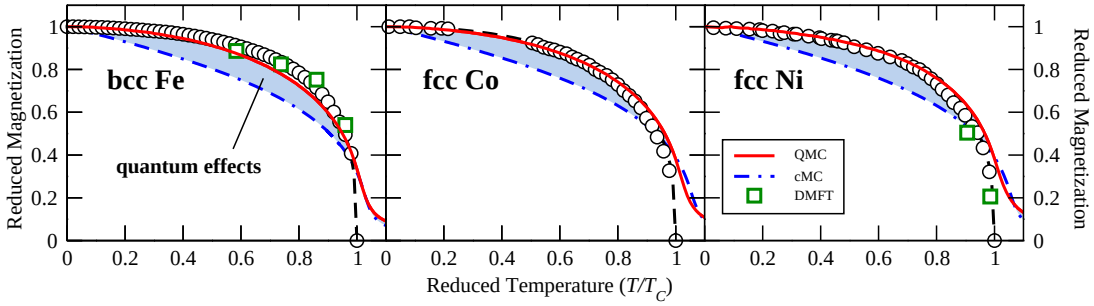

Figure 11: Reduced magnetization $M(t)/M_0$ for the unary ferromagnetic materials Fe, Co, and Ni, using the effective nearest-neighbour model. The results are compared with cMC and DMFT [62] calculations.

note that recently different extensions of classical Heisenberg-like Hamiltonians, which account for longitudinal spin fluctuations (giving raise to a temperature dependence of the effective local magnetic moments), have been proposed and successively applied [63, 64].

3 Heat capacities of selected material systems

While the theoretical approaches outlined in the previous section allow principally to study any thermodynamic quantity, e.g., free energies, enthalpies, entropies, thermal expansion coefficients, isobaric and isochoric heat capacities, and have indeed been used to do it (see e.g., Refs. [21, 29]), we will focus in the following on the isobaric heat capacity. This is the key quantity obtained from calorimetric measurements and one of the cornerstones of constructing thermodynamic phase diagrams. Similar like in the previous section we will first focus on non-magnetic metals and then include magnetic effects.

3.1 Importance of anharmonic contributions at extreme temperatures: A case study for Al

While a thermodynamic description of metals using the quasiharmonic approximation together with electronic excitations is by now a routine approach little has been known regarding the relevance of point defects and anharmonicity. Both contributions are expected to become important at extreme temperatures, i.e., at temperatures where the solid becomes less and less stable against transformations in a new phase (martensitic transitions) or in the liquid phase. Indeed, early speculations about the nature of the relevant excitation mechanism driving the structural instability date back more than 90 years [65]. The methods outlined in Secs. 2.2 and 2.3 provide for the first time the opportunity to study this question directly. Since calorimetric measurements to determine the heat capacity are highly sensitive to sample preparation, measurement geometry, sample holder etc. rather large errors result when comparing, e.g., to diffraction techniques used to measure geometric quantities such as lattice constants, bond length etc.

For the following discussion we will therefore focus on fcc bulk Al, a metallic material that can be produced with high chemical purity as single crystal and for which a large set of precise

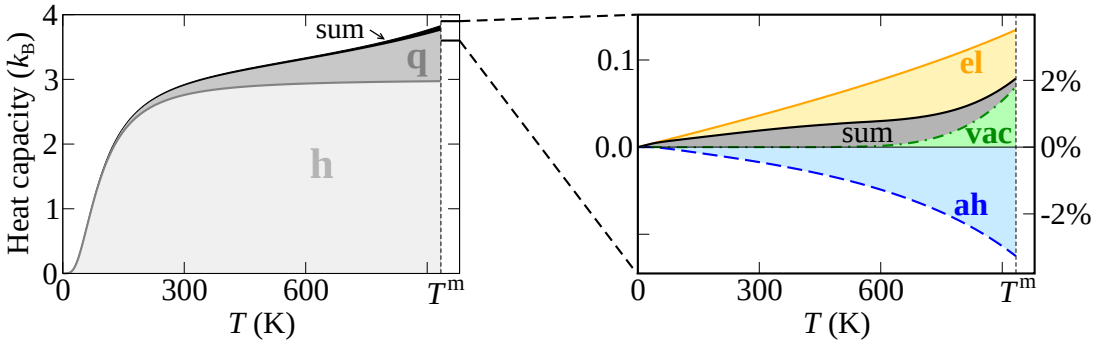

Figure 12: Isobaric heat capacity for aluminium. The figure shows (left) the two major contributions from harmonic and quasiharmonic excitations and (right) a detailed comparison of the remaining contributions coming from explicitly anharmonic vibrations (ah), vacancies (vac) and electronic excitations (el).

experimental data is available. As shown in Fig. 5, already the quasiharmonic approximation together with electronic entropy both LDA and GGA provide a remarkable agreement with the experimental data. Similar as discussed before LDA and GGA provide approximate error bars (bounds) to the experimental data, except when going to temperatures close to the melting point. This behaviour indicates that close to the melting point excitation mechanisms beyond quasiharmonicity and electronic excitations become relevant.

Computing the free energy contributions due to explicit anharmonicity and point defect creation a full analysis becomes possible (Fig. 12). Zooming into the contributions beyond the quasiharmonic approximation (right side of Fig. 12) electronic and vacancy excitations yield the anticipated *positive* contribution to the heat capacity. However, in contrast to previous belief the explicitly anharmonic excitations show the opposite trend resulting in a *negative* contribution. The reason is that a large part of anharmonicity is already contained in the quasiharmonic approximation, making the explicit part only a small (negative) contribution. Since the electronic and the explicit anharmonic contribution largely cancel, the dominant contribution responsible for the almost exponential increase of the heat capacity near the melting temperature is the contribution due to defect formation.

To assess the accuracy of DFT in predicting key thermodynamic quantities such as the heat capacity a comparison with the full experimental data sets, i.e., not the averaged ones usually taken, is highly instructive. Fig. 13b shows that both LDA and GGA results agree well with experiment up to ≈ 600 K, i.e. in a temperature region where the experimental scatter is small. Above 600 K, there is a large scatter in the experimental data making a fair comparison with theory difficult. A general trend is that almost all experiments performed later than 1950 (solid squares in Fig. 13) show a steeper increase towards the melting temperature making the DFT results a lower bound. This trend indicates that unintentional defects/impurities are in the sample giving rise to additional excitation mechanisms [29]. It is interesting to note that theory has reached here a level of accuracy which goes well beyond experimental error bars calling for refined experimental strategies to measure this - for thermodynamic data critical - quantity with higher precision. As mentioned before structural parameters such as lattice constants can be

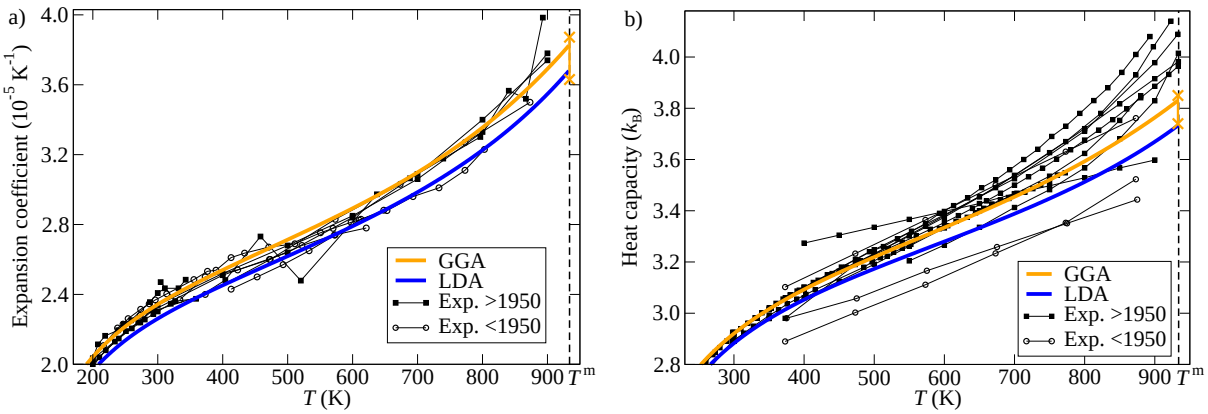

Figure 13: a) Thermal expansion coefficient and b) isobaric heat capacity of aluminium including the electronic, quasiharmonic, anharmonic, and vacancy contribution compared to experiment. The melting temperature T^{m} of Al (933 K) is given by the vertical dashed line. At T^{m}, the crosses indicate the sum of all numerical errors (e.g., pseudo-potential error or statistical inaccuracy; cf. Ref. [22]) in all contributions for GGA. The LDA error is of the same order of magnitude. The figures are adopted from Ref. [29], where also the references for the experimental data can be found.

measured with much higher precision and are therefore an ideal test bed to assess the accuracy of our presently available xc-functionals. We have therefore also studied the thermal expansion coefficient (Fig. 13a). As can be nicely seen including all free energy contributions provides an amazing agreement with experiment up to the melting point. Even details close to the melting temperature are correctly reproduced.

3.2 Cementite above the Curie temperature

Using the concepts explained in Sec. 2.4, thermodynamic properties can also be obtained for magnetic materials. The effective nearest-neighbour approach in combination with vibrational

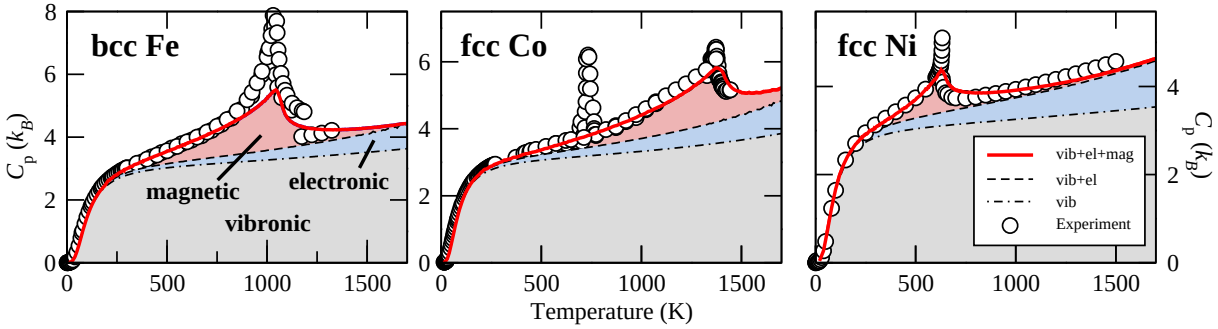

Figure 14: Isobaric heat capacity for the unary ferromagnetic materials Fe, Co, and Ni, using the effective nearest-neighbour model. The complete *ab initio* results including all free energy contributions (red, solid lines), the result from the vibrational analysis only (dash-dotted lines) and the results from a combined vibrational and electronic analysis (dashed lines) are shown.

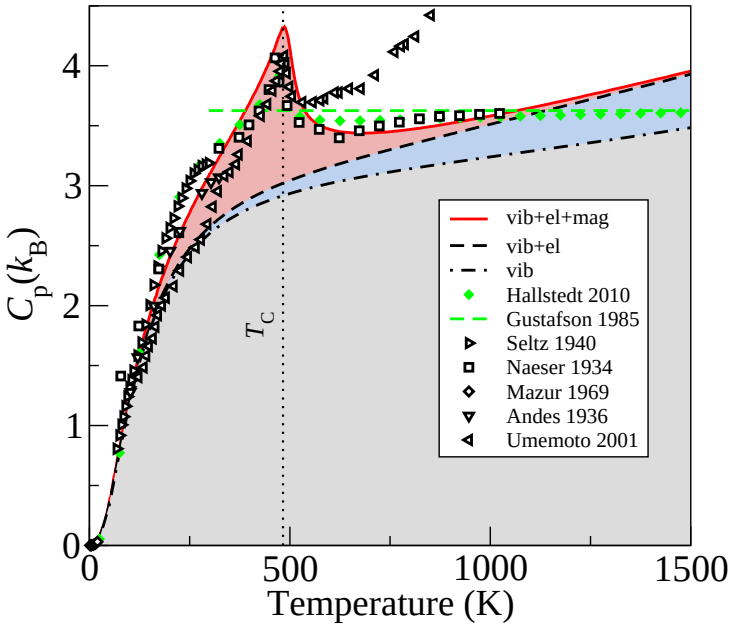

Figure 15: Calculated heat capacity of cementite in comparison with available experimental data (open symbols) and thermodynamic assessments (filled symbols). The calculated electronic and magnetic contributions to the heat capacity are shown in shaded orange and grey correspondingly.

and electronic excitations has successfully been applied to the unary ferromagnetic materials Fe, Co, and Ni to obtain their magnetization curves (Sec. 2.4). The corresponding heat capacities are shown in Fig. 14. The results for the heat capacity of Fe are almost identical to those displayed in Fig. 9. The excellent agreement with the experimental data for Ni may appear particularly surprising, since in contrast to Fe and Co, where the local magnetic moment remains almost unaffected by the magnetic transition, the local magnetic moments of Ni are often reported to drastically reduce [63]. An extension of the Heisenberg model such that longitudinal fluctuations are considered appears therefore mandatory and has certainly a large influence on magnetic quantities like the Curie temperature. The results for Ni, however, indicate that such an extension does not affect the universality of the quantum-mechanical corrections of the heat capacity used in the present approach.

Based on the excellent predictive power found for unary magnetic systems, the approach has been extended and applied to technologically more relevant systems. A prominent example which we will discuss in the following is that of cementite, Fe_3C. This carbide is a key precipitate phase in Fe-based materials and often introduced on purpose to strengthen the mechanical properties of steels. In contrast to its technological importance its thermodynamic description, e.g., in various CALPHAD approaches, is very limited. For example, in the assessment of Gustafson from 1985 [2], which is the basis for well established databases, the heat capacity of cementite was treated as a constant (see green, dashed line in Fig. 15), whereas experiments (black symbols) show a much more complex behaviour. One reason for the rather pragmatic CALPHAD treatment of Fe_3C might be the large scatter in the experimental data, which is mainly due to the lack of sufficiently pure cementite samples and the unavoidable mixture with ferrite and other carbides. The scatter

becomes particularly apparent in the temperature range above the Curie temperature (dotted line in Fig. 15).

This case is typical for many material systems, and supplementing (assessing) experimental datasets with results of first-principles calculations becomes particularly appealing. Correspondingly, the methods described in this article have been employed for computing the vibrational, electronic and magnetic free energy contribution of Fe_3C.[66] The resulting heat capacity is shown in Fig. 15 (red line). It reproduces the findings of some of the experiments remarkably well, indicating at the same time clearly, which experiments are deviating from the expected behaviour. In particular in the high-temperature limit a clear statement about the performance of the various experimental datasets becomes possible, allowing a critical assessment and weighting of the experimental data as needed in a thermodynamic assessment. These insights have indeed been used by the CALPHAD community for an improved description of the Fe-Mn-C phase diagram by Hallstedt et al. [66].

4 Application to steel design

In the following we will briefly discuss a prominent example in actual steel design, for which an accurate determination of thermodynamic quantities is crucial and can presently not be obtained experimentally in the needed detail. As outlined in the introduction, modern high strength steels are heavily relying on sophisticated mechanisms that are activated by deformations and/or temperature and that require a careful control of the chemical composition. A critical quantity for designing new steel grades based on these concepts is the determination of intrinsic stacking fault energies (see Sec. 1.1). As mentioned before, small changes of the SFE, in the order of a few mJ/m^2, can be essential for the dominant deformation mechanism (TRIP vs. TWIP) in the considered steels. Using the methods sketched in Sec. 2, changes (in particular due to temperature) in this order of magnitude can now be resolved.

Essentially two different *ab initio* concepts are available for a determination of SFEs. On the one hand, one can explicitly set up stacking faults in a supercell calculation, which is often generalized to the complete energy surface (γ surface) of two half fcc crystals displaced along a (111) plane with respect to each other. In this way, one additionally gets access to transition paths and energy barriers relevant for the creation of stacking faults. An alternative approach to obtain the intrinsic SFE is the axial next-nearest-neighbour Ising (ANNNI) model [67]. In this approach, the energy of the crystal with a stacking fault is expanded into a sum of energies of periodically repeated stacking sequences of (111) layers. It turns out that in first order of the ANNNI model the SFE is proportional to the energy difference of the hcp and the fcc phase, provided both phases have been evaluated at the same volume.

This knowledge reduces a complex materials design problem to the determination of free energies, considered in this article. First *ab initio* studies using these concepts have mainly focused on the prediction of chemical trends for the SFE of steels. Clearly, any attempt in this direction needs to additionally include the chemical and paramagnetic disorder, which is relevant for high temperatures. The coherent potential approximation (CPA) as well as the concept of special quasi random structures (SQS) have turned out to be very suitable for this purpose. In particular

the magnetic configuration and its temperature dependence turned out to be decisive for steels. Taking care of this, it was for example possible to proof with *ab initio* methods an increase by almost 30 mJ m^{-2} in the SFE of high-Mn steels due to the presence of 6 at.% Al [68].

For C, an interstitial alloying element which is present in practically all steels, the situation turns out to be even more interesting: The assumption of a completely homogeneous C distribution yields a drastic increase of the SFE also in this case. Consequently, there is a strong thermodynamic driving force for C to move away from the region of the stacking fault. Since C is an interstitial atom, an increase of the temperature by some 100 K can already be sufficient for C to overcome the kinetic barriers and to reach thermodynamic equilibrium. As a result, the SFE region will be free of C and the SFE becomes almost independent of the C contents in the steel. Using this *ab initio* based insight, large discrepancies in experimental values for SFEs have recently been resolved [69].

Nevertheless, temperature does not only play a role in terms of magnetic configurations or kinetic barriers, also the explicit temperature dependence of the SFE turns out to be significant. With the ANNNI model and its relation to the free energy of the fcc and hcp phase, this temperature becomes directly accessible for *ab initio* methods when using the thermodynamic methods discussed above. Using this approach we have recently shown that the SFE of iron changes by more than 100 mJ/m^2 over a temperature range of 1000 K [70]. This prediction is highly relevant for the temperature ranges at which the TWIP effect can be expected.

Another important deformation mechanism in high-Mn steels, mentioned in the introduction, is the TRIP effect. It is related to a martensitic phase transition, in this case caused by a mechanical load. However, also temperature driven martensitic phase transitions are highly relevant for the mechanical properties of materials. A prominent example are shape memory alloys (SMA), such as NiTi. They make use of the fact that the martensitic phase, being stable below the transition temperature, has a lower symmetry than the austenitic phase. Therefore, any macroscopic deformation of the material in the martensitic phase is easily possible by changing between different microscopic variants, whereas the heating to the austenitic phase will always ensure a return of the original shape. In some magnetic SMA the transition can also be controlled by magnetic fields, which is particularly attractive for applications with switching frequencies in the kHz regime.

Having access to the free energies of all relevant steel phases, this kind of martensitic phase transitions become accessible for *ab initio* methods. The concepts described in this article have, e.g., recently been used to predict the sequence of phase transitions in the Heusler alloy Ni_2MnGa [23], including the existence of a pre-martensitic phase. Applying this approach made it not only possible to resolve the delicate interplay between vibrational and magnetic degrees of freedom in this material system, but also to make simulations about the change of the martensitic transition temperature with the chemical composition. Since the transition temperature of Ni_2MnGa is with 200 K much too low for practical applications of the material, the observed increase of the transition temperature, e.g., by replacing Mn partially by Ni is of great importance for the production of devices.

Recently, also the investigations on Heusler structures became highly relevant for steel design. In some novel steel concepts (maraging TRIP, see Fig. 1), a very high strength level is obtained

by the formation of intermetallic nanoparticles in the martensite during aging. Modern experimental techniques, such as atom probe tomography, have recently indicated that some of these particles could, e.g., have the $L2_1$ structure of Ni_2MnAl [71, 72]. The formation and relevance of these precipitates is part of an ongoing research, combining state-of-the-art theoretical and experimental techniques.

5 Conclusions and Outlook

A major aim of the present article is to show the status, the progress that has been made over the last years but also the challenges we still face in using density functional theory which originally has been developed as a T=0 K ground state methodology to compute thermodynamic properties of real world materials with an accuracy needed for engineering and design. We purposely biased our focus on metallic alloys with emphasize on steels since these materials are the basis for a wide range of engineering applications. From a methodological point metals do not suffer from the infamous bandgap problem of DFT, providing a sound basis for comparing the advanced approaches developed for computing the various free energy contributions with experiment.

The possibility to analyse and identify chemical trends is a major advantage of *ab initio* approaches. In contrast to absolute quantities deficiencies due to the approximate nature of the xc-functional become less relevant since only relative values need to be considered. This well established finding can now be extended to thermodynamic properties. With the portfolio of methods described in this article it becomes possible to address a wide variety of scientifically and economically pressing issues in materials and steel design, which are related to finite temperature thermodynamics. While a first major step has been done, further methodological developments in particular with respect to the treatment of complex magnetic alloys, the consideration of non-adiabatic interactions and the multi-scale connection towards micro-structural features are still necessary.

Acknowledgments

Funding by the collaborative research center, SFB 761 "Stahl-*ab initio*", of the Deutsche Forschungsgemeinschaft and the Interdisciplinary Centre for Materials Simulation (ICAMS), which is supported by ThyssenKrupp AG, Bayer MaterialScience AG, Salzgitter Mannesmann Forschung GmbH, Robert Bosch GmbH, Benteler Stahl/Rohr GmbH, Bayer Technology Services GmbH and the state of North-Rhine Westphalia, as well as the European Commission in the framework of the European Regional Development Fund (ERDF) is gratefully acknowledged. Part of this work was performed under the auspices of the U.S. Department of Energy by Lawrence Livermore National Laboratory under Contract DE-AC52-07NA27344.

References

[1] D. Raabe, D. Ponge, O. Dmitrieva and B. Sander, Adv. Eng. Mater. **11**, 547 (2009).

[2] A. Fernández Guillemet and P. Gustafson, High Temp. High Press. **16**, 591 (1985).

[3] G. Frommeyer, U. Brüx and P. Neumann, ISIJ Int. **43**, 438 (2003).

[4] L. Krüger, L.W. Meyer, U. Brüx, G. Frommeyer and O. Grässel, J. Phys. IV page 189 (2003).

[5] Y. A. Chang, S. Chen, F. Zhang, X. Yan, F. Xie, R. Schmid-Fetzer and W. A. Oates, Prog. Mater. Sci. **49**, 313 (2004).

[6] P. E. A. Turchi, I. A. Abrikosov, B. Burton, S. G. Fries, G. Grimvall et al., CALPHAD **31**, 4 (2007).

[7] M. Palumbo, T. Abe, C. Kocer, H. Murakami and H. Onodera, CALPHAD **34**, 495 (2010).

[8] C. Zacherl, J. Saal, Y. Wang and Z.K. Liu, Intermetallics **18**, 2412 (2010).

[9] A. Chari, A. Garay and R. Arroyave, CALPHAD **34**, 189 (2010).

[10] A. Durga and K.C. Hari Kumar, CALPHAD **34**, 200 (2010).

[11] G. Cacciamani, A. Dinsdale, M. Palumbo and A. Pasturel, Intermetallics **18**, 1148 (2010).

[12] C. Tang, Y. Du, J. Wang, H. Zhou, L. Zhang, F. Zheng, J. Lee and Q. Yao, Intermetallics **18**, 900 (2010).

[13] N. D. Mermin, Phys. Rev. **137**, A1441 (1965).

[14] R. Kikuchi, Phys. Rev. **81**, 988 (1951).

[15] J. M. Sanchez, F. Ducastelle and D. Gratias, Physica A **128**, 334 (1984).

[16] H. Hellmann, *Einführung in die Quantenchemie*, Deuticke, Leipzig (1937).

[17] R. P. Feynman, Phys. Rev. **56**, 340 (1939).

[18] P. Giannozi, S. Gironcoli, P. Pavone and S. Baroni, Phys. Rev. B **43**, 7231 (1991).

[19] G. Kresse and J. Furthmüller, Phys. Rev. B **54**, 11169 (1996).

[20] G. Kresse and D. Joubert, Phys. Rev. B **59**, 1758 (1999).

[21] B. Grabowski, T. Hickel and J. Neugebauer, Phys. Rev. B **76**, 024309 (2007).

[22] B. Grabowski, *Towards ab initio assisted materials design: DFT based thermodynamics up to the melting point*, PhD thesis Universität Paderborn (2009).

[23] M. A. Uijttewaal, T. Hickel, J. Neugebauer, M. E. Gruner and P. Entel, Phys. Rev. Lett. **102**, 035702 (2009).

[24] Y.-C. Hsue J.-H. Lee and A. J. Freeman, Phys. Rev. B **73**, 172405 (2006).

[25] J. P. Perdew, A. Ruzsinszky, G. I. Csonka, O. A. Vydrov, G. E. Scuseria, L. A. Constantin, X. Zhou and K. Burke, Phys. Rev. Lett. **100**, 136406 (2008).

[26] Y. S. Touloukian and E. H. Buyco, *Specific Heat - Metallic Elements and Alloys*, In *Thermophysical Properties of Matter* volume 4. IFI/Plenum, New York (1970).

[27] M. Forsblom, N. Sandberg and G. Grimvall, Phys. Rev. B **69**, 165106 (2004).

[28] D. Alfe, Phys. Rev. B **79**, 060101 (2009).

[29] B. Grabowski, L. Ismer, T. Hickel and J. Neugebauer, Phys. Rev. B **79**, 134106 (2009).

[30] A. Dick. Alexey L. Ismer S. Boeck C. Freysoldt and J. Neugebauer, Comput. Phys. Commun. **182**, 543 (2010).

[31] P. Blaha, K. Schwarz, G. Madsen, D. Kvasnicka and J. Luitz, *WIEN2k, An Augmented Plane Wave + Local Orbitals Program for Calculating Crystal Properties*, Technische Universität Wien, Austria (2001).

[32] M. J. Gillan, J. Phys. Condens. Matter **1**, 689 (1989).

[33] A. Satta, F. Willaime and S. de Gironcoli, Phys. Rev. B **57**, 11184 (1998).

[34] A. Satta, F. Willaime and S. de Gironcoli, Phys. Rev. B **60**, 7001 (1999).

[35] K. M. Carling, G. Wahnström, T. R. Mattsson, A. E. Mattsson, N. Sandberg et al., Phys. Rev. Lett. **85**, 3862 (2000).

[36] K. M. Carling, G. Wahnström, T. R. Mattsson, N. Sandberg and G. Grimvall, Phys. Rev. B **67**, 054101 (2003).

[37] B. Grabowski, T. Hickel and J. Neugebauer, Phys. Status Solidi B **248**, 1295 (2011).

[38] P. E. Blöchl, Phys. Rev. B **50**, 17953 (1994).

[39] D. E. Turner, Z. Z. Zhu, C.-T. Chan and K.-M. Ho, Phys. Rev. B **55**, 13842 (1997).

[40] R. Pawellek, M. Fähnle, C. Elsässer, K.-M. Ho and C.-T. Chan, J. Phys. Condens. Matter **3**, 2451 (1991).

[41] H. M. Polatoglou, M. Methfessel and M. Scheffler, Phys. Rev. B **48**, 1877 (1993).

[42] T. Korhonen, M. J. Puska and R. M. Nieminen, Phys. Rev. B **51**, 9526 (1995).

[43] G. Lucas and R. Schäublin, Nucl. Instr. Meth. Phys. Res. B **267**, 3009 (2009).

[44] R. O. Simmons and R. W. Balluffi, Phys. Rev. **117**, 52 (1960).

[45] T. Hehenkamp, J. Phys. Chem. Solids **55**, 907 (1994).

[46] X. Sha and R. E. Cohen, Phys. Rev. B **73**, 104303 (2006).

[47] C. Friedrich, S. Blügel and A. Schindlmayr, Phys. Rev. B **81**, 125102 (2010).

[48] S. V. Halilov, A. Y. Perlov, P. M. Oppeneer and H. Eschrig, Europhys. Lett. **39**, 91 (1997).

[49] L. M. Sandratskii, Adv. Phys. **47**, 91 (1998).

[50] F. Körmann, A. Dick, T. Hickel and J. Neugebauer, Phys. Rev. B **78**, 033102 (2008).

[51] Y. S. Touloukian, R.K. Kirby, R.E. Taylor and P.D. Desai, In *Thermophysical Properties of Matter* volume 12. IFI/Plenum, New York (1975).

[52] D.C. Wallace, P.H. Sidles and G.C. Danielson, J. Appl. Phys. **31**, 168 (1960).

[53] A.F. Albuquerque, F. Alet, P. Corboz, P. Dayal, A. Feiguin, S. Fuchs, L. Gamper, E. Gull, S. Gürtler, A. Honecker, R. Igarashi, M. Körner, A. Kozhevnikov, A. Läuchli, S.R. Manmana, M. Matsumoto, I.P. McCulloch, F. Michel, R.M. Noack, G. Pawlowski, L. Pollet, T. Pruschke, U. Schollwöck, S. Todo, S. Trebst, M. Troyer, P. Werner and S. Wessel, J. Magn. Magn. Mater. **310**, 1187 (2007).

[54] N.N. Bogolyubov and S.V. Tyablikov, Soviet. Phys.-Doklady **4** (1959).

[55] A.W. Sandvik and J. Kurkijärvi, Phys. Rev. B **43**, 5950 (1991).

[56] H. G. Evertz, Adv. Phys. **52**, 1 (2003).

[57] P. Henelius and A.W. Sandvik, Phys. Rev. B **62**, 1102 (2000).

[58] E. Y. Loh, J. E. Gubernatis, R. T. Scalettar, S. R. White, D. J. Scalapino and R. L. Sugar, Phys. Rev. B **41**, 9301 (1990).

[59] F. Körmann, A. Dick, T. Hickel and J. Neugebauer, Phys. Rev. B **81**, 134425 (2010).

[60] F. Körmann, A. Dick, T. Hickel and J. Neugebauer, Phys. Rev. B **83**, 165114 (2011).

[61] F. Körmann, A. Dick, T. Hickel and J. Neugebauer, Phys. Rev. B **79**, 184406 (2009).

[62] A. I. Lichtenstein, M. I. Katsnelson and G. Kotliar, Phys. Rev. Lett. **87**, 067205 (2001).

[63] A. V. Ruban, S. Khmelevskyi, P. Mohn and B. Johansson, Phys. Rev. B **75**, 054402 (2007).

[64] M. Yu. Lavrentiev, D. Nguyen-Manh and S. L. Dudarev, Phys. Rev. B **81**, 184202 (2010).

[65] M. Born and E. Brody, Z. Phys. **6**, 132 (1921).

[66] B. Hallstedt, D. Djurovic, J. von Appen, R. Dronskowski, A. Dick, F. Körmann, T. Hickel and J. Neugebauer, CALPHAD **34**, 129–133 (2010).

[67] W. Selke, Phys. Rep. **170**, 213 (1988).

[68] T. Gebhardt, D. Music, M. Ekholm, I.A. Abrikosov, L. Vitos, A. Dick, T. Hickel, J. Neugebauer and J. M. Schneider, J. Phys.: Condens. Matter **23**, 246003 (2011).

[69] A. Abbasi, A. Dick, T. Hickel and J. Neugebauer, Acta Mat. **59**, 3041 (2011).

[70] A. Dick, T. Hickel and J. Neugebauer, in preparation (2011).

[71] J. Millan, D. Ponge, D. Raabe, P. Choi and O. Dmitrieva, steel research int. **82**, 137 (2011).

[72] Y. Heo, M. Takeguchi, K. Furuya and H. Lee, J. Electr. Micr. **59**, 35 (2010).